7-11-2023

A thermodynamics-based versatile evapotranspiration estimation method of minimum data requirement for water resources investigations

Jozsef Szilagyi

Richard D. Crago

Journal of Hydrology 624 (2023) 129917

Contents lists available at ScienceDirect

Journal of Hydrology

journal homepage: www.elsevier.com/locate/jhydrol

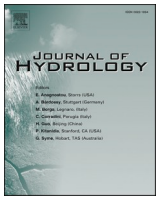

Research papers

A thermodynamics-based versatile evapotranspiration estimation method of minimum data requirement for water resources investigations

Jozsef Szilagyi [a,b,*], Richard D. Crago [c]

[a] National Laboratory for Water Science and Water Security, Department of Hydraulic and Water Resources Engineering, Budapest University of Technology and Economics, Muegyetem Rkp. 1-3, Budapest H-1111, Hungary
[b] Conservation and Survey Division, School of Natural Resources, University of Nebraska-Lincoln, 3310 Holdrege St., Lincoln, Nebraska, USA
[c] Department of Civil and Environmental Engineering, Bucknell University, Lewisburg, PA, USA

ARTICLE INFO

This manuscript was handled by Dr Marco Borga, Editor-in-Chief, with the assistance of Murray Peel, Associate Editor

Keywords:
Complementary relationship of evaporation
Water resources
Water balance
Climate change

ABSTRACT

A recent, two-parameter version of the thermodynamically derived complementary relationship (CR) of evaporation has been tested on a monthly basis at 124 FLUXNET stations around the globe. Local, station-by-station calibration explained 91% (R^2) of the variance in eddy-covariance (EC) obtained latent-heat fluxes with the same Nash-Sutcliffe efficiency (NSE) value. When the dimensionless Priestley-Taylor parameter (α) was expressed as a universal function (f) of the estimated wet-environment air temperature (T_w), station-by-station calibration of the single dimensionless parameter, b (accounting for moisture advection), yielded an R^2 value of 87% and NSE of 86%. Global calibration (all stations at once) of the two-parameter CR version yielded $R^2 = 82\%$ and NSE = 81%, while the single-parameter version produced $R^2 = 81\%$ and NSE = 79%. With a representative value (between the locally calibrated mode and mean) of b set equal to two, the thus, calibration-free CR still maintained an R^2 of 80% and NSE of 78%, which is significantly better than Morton's calibration-free WREVAP model (i.e., 71% and 55%, respectively). The advantage of the current CR model is that it can be employed in a fully calibration-free mode, similar to WREVAP, yet with available EC measurements or water-balance derived latent-heat fluxes the single [b, when $\alpha = f(T_w)$ is chosen] or two parameters (α and b) of the model can be easily calibrated within the respective 1 – 1.32 and 1 – 10 intervals, for further improved performance.

1. Introduction

In our fast-changing climate of the Earth, with more frequent droughts, heatwaves, extreme precipitation and floods (often at the same location), and with global warming already exceeding 1.1 °C above the pre-industrialized base line (WMO, 2021), (re)allocation of water resources is an ever pressing problem. Just consider the prominent examples of Lake Aral in Central-Asia (Huang et al., 2022), Lake Urmia in Iran (Rezaei and Gurdak, 2020), or Lake Chad in Sub-Saharan Africa (Mahmood and Jia, 2019), places where current lake surface areas are just a fraction of their original extent due to climate change and/or mismanagement of the water resources in the corresponding watersheds. The ongoing dispute over the Nile water between Egypt and Ethiopia (Ayyad and Khalifa, 2021), the fast dwindling water resources in the reservoirs of California and the South-West in the USA (Carlowicz, 2022) or, the dramatic situation of Cape Town (population of 4.6 million) in South Africa when in 2021 the city was only days away from running out of water as its major water-supply reservoirs had run almost completely dry (Maxmen, 2018), are other prime examples of globally occurring water resource management issues often severely exacerbated by climate change.

In a classical civil engineering approach, evapotranspiration (ET) is considered as a loss term, since precipitation less ET over an extended period (i.e., year, decade) constitutes water remaining on the land as direct runoff or recharge to the groundwater for management and control. There is a recent tendency to retain as much water as possible on the land (and thus eventually reduce runoff due to increased ET) so that enough water would be available for societal use and accessible to the ecosystems during extended drought periods (Susnik et al., 2022; Ward, 2022). However, such retention of water will certainly create its own problems: altered streamflow regime and the consequent morphological changes (including sediment load) in the channel (Kaisheng, 2022), vegetational/ecological changes in the flood-plain (Palmer et al., 2014), as well as possible declines in groundwater levels in areas adjacent to

* Corresponding author.
E-mail address: szilagyi.jozsef@emk.bme.hu (J. Szilagyi).

https://doi.org/10.1016/j.jhydrol.2023.129917
Received 13 January 2023; Received in revised form 24 April 2023; Accepted 4 July 2023
Available online 11 July 2023

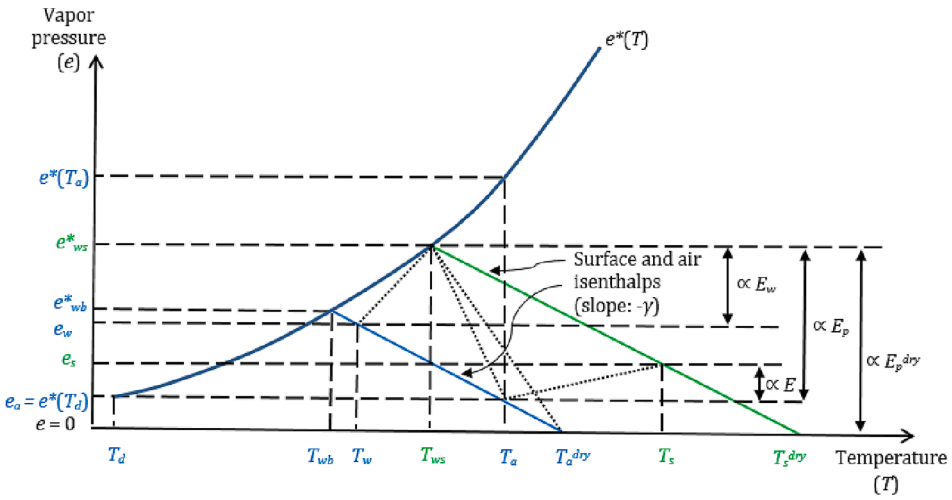

Fig. 1. Saturation vapor pressure (e^*) curve, air (blue) and surface (green) isenthalps (Szilagyi, 2021; Crago and Qualls, 2021) during a full drying-out of the environment from completely wet (where the isenthalps join the saturation vapor pressure curve) to a completely dry state (where vapor pressure is zero). The vertical projections (denoted by the vertical two-way arrows) of the dotted lines are proportional (∝) to the different evaporation terms ($E \le E_w \le E_p \le E_p^{dry}$) discussed below. The green-colored variables with an 's' in their subscript denote surface values. T_d and T_{wb} are the dew-point and wet-bulb temperatures, respectively. See below and also Szilagyi (2021) for additional definitions and explanation. (For interpretation of the references to colour in this figure legend, the reader is referred to the web version of this article.)

streams (la Cecilia and Camporese, 2022) with its ensuing further consequences, just to name a few.

Certainly, all these civil/environmental engineering efforts to modify components of the hydrological cycle on a regional or sub-regional scale, require an accurate estimate of the ET rates over the area in question (typically a watershed as a naturally emerging building block of terrestrial hydrological processes) at time increments usually not shorter than a month.

Although there is a plethora of ET models to choose from, there are very few available that would not require some kind of a calibration. Even those models that are calibration-free, typically contain numerous empirical parameters already pre-calibrated and may depend on complex soil (e.g., physical type, hydraulic properties, thickness, layering, clay content, etc.) and biophysical parameters (land cover, rooting depth, land use) that may change abruptly (due to e.g., land-use change) or vary on a longer time scale as a result of climate change, making periodical recalibration of the parameters involved a necessity.

An ET estimation approach that integrates all these possible changes by inherently accounting for the complex land–atmosphere interactions involved, requires a minimum number of input variables and does not need periodic recalibration is certainly worthy of further investigation. The complementary relationship (CR) of evaporation, first recognized by Bouchet (1963) is such an approach. Complementarity means that as the land on a regional extent dries out, actual ET rates, E, decrease, while potential ET rates, E_p, from a plot-sized wetland or rather from a hypothetical wet surface within the drying region, concurrently increase. As a result, by observing/estimating E_p, E can be predicted via the CR. Such a relationship exists because the atmosphere adjusts itself to the moisture status of the underlying land via the consequent ET rates as a product of complex land–atmosphere interactions (through hard-to-quantify physical/biological/chemical processes within the vegetation and the soil) and doing so directly affects the concurrent E_p rates. The latter predominantly depend only on atmospheric variables and available energy (Q_n) at the land surface, as access to water is not limited therefore soil hydraulic processes and the complex regulatory mechanism of the vegetation do not have a role. The atmospheric variables that control the E_p rates include air temperature (T_a), humidity (frequently expressed via the vapor pressure deficit, *VPD*), and wind speed (u), while Q_n is net radiation (R_n) at the surface less heat conduction (G) into the ground, all of these variables measured over the drying land (not affected by the presence of the wet surface). *VPD* is the difference between the saturation, e^* (=6.108exp[17.27T_a / {237.3 + T_a}]) and actual, e_a, vapor pressure. In the present, so-called *Teten's* formula (Stull, 1988), T_a is specified in °C and e^* results in hPa.

In the following a recent, thermodynamically-derived version of the CR (Szilagyi et al., 2022) is to be applied with monthly input data coming potentially from altogether 171 FLUXNET stations (Pastorello et al., 2020) around the globe. CR model performance will be tested with respect to the i) possible linear, polynomial or power-function relationship of its dimensionless variables, and; ii) number of parameters (from two to none) to calibrate either globally and/or locally. Such a systematic testing with eddy-covariance measured data has not been performed before. A novel calibration-free version of the CR will eventually be proposed for general water resources management applications when calibration is not possible due to lack of measured or water-balance derived ET rates.

2. Theory

2.1. Theoretical background of the thermodynamics-based CR

Crago and Qualls (2021), as well as Szilagyi (2021), aided by the pioneering work of Monteith (1981) realized that when the air is cooled down by evaporation during an adiabatic and isobaric (i.e., isenthalpic) process, the air (T_a, e_a) and surface (T_s, e_s) value pairs (coordinates of the vapor pressure – temperature state diagram) move along two largely parallel isenthalpic lines (Fig. 1). In this isenthalpic approach it is implicitly assumed that Q_n would not change either i) during drying/wetting of the environment at a fixed location (i.e., temporal view), or; ii) among locations experiencing different stages of drying/wetting but sharing the same Q_n value at the same fixed time (i.e., spatial view). The temporal view can be met only by invoking a certain compensatory effect of changing cloudiness with the wetness of the environment to changes in surface temperature. As the land dries out, its surface temperature increases and so does its outgoing thermal radiation. But concurrently, incoming short-wave radiation increases as well due to reduced cloudiness, possibly compensating for the increased thermal energy loss, and vice-versa during wetting. In contrast, the spatial view does not require any assumption about the temporal evolution of Q_n (since it is a spatial 'snapshot') therefore it is more comprehensive. Also, it's better suited for monthly time-steps where it is rare that Q_n would remain unchanged between consecutive months, at least in mid-latitudes, therefore the isenthalps the air (T_a, e_a) and surface (T_s, e_s) value pairs are located on change from month to month.

Szilagyi (2021) by assuming that the relative speed at which the (T, e) coordinates traverse the isenthalps stays constant in time, while Crago and Qualls (2021) from dimensional considerations, derived the following non-dimensional form of the CR

$$\frac{E}{E_w} = \frac{E_p^{dry} - E_p}{E_p^{dry} - E_w} \tag{1}$$

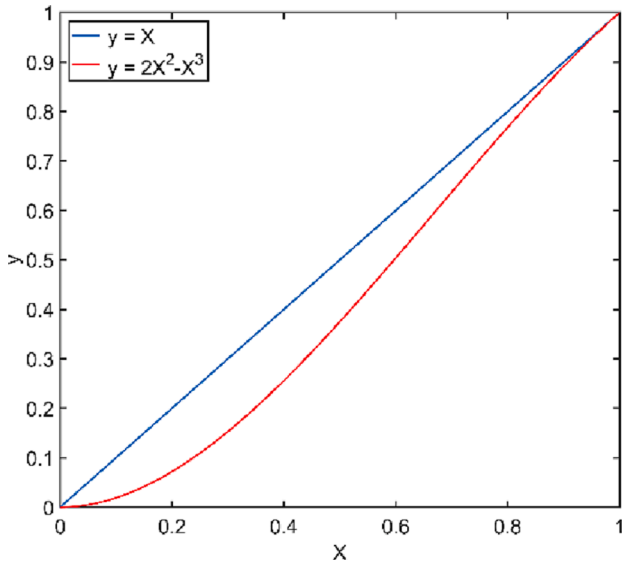

Fig. 2. The linear and polynomial CR relationships between $y = E\,E_p^{-1}$ and $X = w_i\,E_w\,E_p^{-1}$.

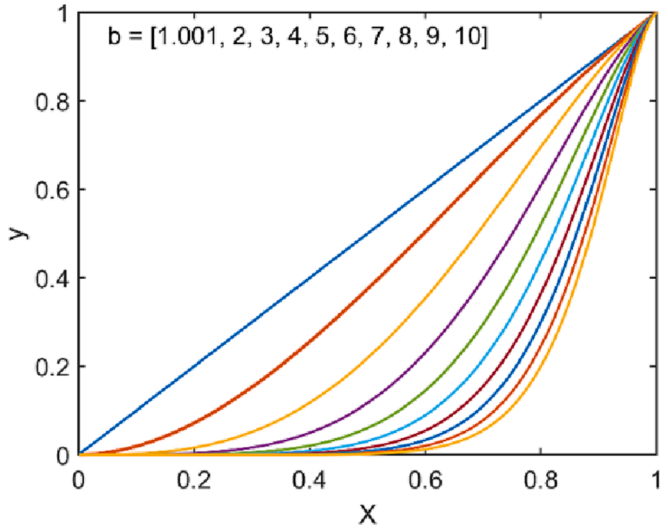

Fig. 3. Graphical representation of Eq. (9) for $1 < b \leq 10$. The polynomial of Eq. (7) ($b \equiv 2$ in Eq. (9)) is the heavier red line. (For interpretation of the references to colour in this figure legend, the reader is referred to the web version of this article.)

The right-hand-side of Eq. (1) is similar to the Normalized Difference Temperature Index (NDTI) of McVicar and Jupp (2002) where the evaporation terms are represented with the corresponding Advanced Very High Resolution Radiometer (AVHRR) measured (for E_p) or Resistance Energy Balance Model (REBM) inverted surface temperatures (for E_p^{dry} and E_w). The clear advantage of Eq. (1) over the NDTI approach is that it does not need remote sensing data nor additional covariates for obtaining E.

E_p can be specified e.g., by the Penman (1948) equation as

$$E_p = \frac{\Delta Q_n}{\Delta + \gamma} + \frac{\gamma f_u [e^*(T_a) - e_a]}{\Delta + \gamma} \tag{2}$$

where Δ [$= 4098e^*(T_a + 237.3)^{-2}$] denotes the slope of the saturation vapor pressure curve (hPa $^\circ C^{-1}$) at the measured air temperature, T_a. The empirical wind function, f_u (mm d^{-1} hPa^{-1}), is traditionally formulated (Brutsaert, 1982) as $f_u = 0.26(1 + 0.54u_2)$. Here u_2 (m s^{-1}) is the horizontal wind speed at 2-m above the ground/canopy surface and can be estimated by a power function (Brutsaert, 1982) from measurements (u_h) at h meters above the surface as $u_2 = u_h\,(2 / h)^{1/7}$, and $\gamma = c_p p\,(0.622L)^{-1}$ is the psychrometric constant, where c_p the specific heat of air under constant pressure, L the latent heat of vaporization and p atmospheric pressure. E_p^{dry} is the theoretical maximum value of E_p when the air/land becomes completely devoid of moisture (i.e., e_a is zero). The air temperature when this would happen results from the slope of the isenthalps as $T_a^{dry} = T_a + e_a / \gamma$. E_w in Eq. (1) is E_p under completely wet environmental conditions and is often estimated by the Priestley and Taylor (1972) equation as

$$E_w = \alpha \frac{\Delta(T_w) Q_n}{\Delta(T_w) + \gamma} \tag{3}$$

where α is the Priestley-Taylor parameter and accounts for the fact that even under perfectly wet conditions (i.e., over the oceans) the air stays rarely saturated over a daily or longer period, therefore the second term in Eq. (2) does not vanish. An $\alpha > 1$ value incorporates the effect of that second (so-called aerodynamic) term of Eq. (2) into the first, so-called energy term, under wet-environmental conditions. The wet-environment air temperature, T_w, can be estimated by the wet-surface temperature, T_{ws}, provided the latter is capped by T_a, as the wet-environment air temperature cannot be higher than T_a (under the same Q_n) due to the cooling effect of evaporation, while T_{ws} can (Szilagyi and Jozsa, 2008; Szilagyi, 2014), by the following equation

$$\frac{Q_n - E_p}{E_p} = \gamma \frac{T_{ws} - T_a}{e^*(T_{ws}) - e_a} \tag{4}$$

which is implicit for T_{ws}, requiring some iterations to solve.

The right-hand-side of Eq. (1) behaves as a wetness index (w_i); its value is zero when the environment is completely dry ($E_p = E_p^{dry}$) and unity when it is completely wet ($E_p = E_w$). Actual evaporation rates thus can be expressed as

$$E = w_i E_w \tag{5}$$

or, in another non-dimensional form (Crago et al., 2016; Szilagyi et al., 2017) as

$$y \equiv \frac{E}{E_p} = \frac{w_i E_w}{E_p} \equiv X \tag{6}$$

The advantage of Eq. (6) over Eq. (1) is in the improved behaviour of its nonlinear version below.

As the environment dries out, the effect of external moisture admixing (in the form of direct horizontal moisture transport from nearby wetter areas, such as large lakes or a sea, or as entrainment of free tropospheric air) into the daytime growing convective boundary layer may become gradually stronger with the possibility of fully decoupling the moisture content of the air from that of the underlying land (Szilagyi et al., 2022). When that happens, changes in X of Eq. (6) will not cause any corresponding change in E and thus in y, i.e., i) $dy / dX \to 0$ as $X \to 0$. The polynomial satisfying this boundary condition (BC), plus the other three BCs implicit in Eq. (6), i.e., ii) $y = 0$ when $X = 0$; iii) $y = 1$ when $X = 1$; iv) $dy / dX = 1$ at $X = 1$; takes the form (Szilagyi et al., 2017; Ma and Szilagyi, 2019; Szilagyi, 2021)

$$y = 2X^2 - X^3 \tag{7}$$

similar to Brutsaert's (2015) nonlinear formulation who defined X differently, without thermodynamic considerations. As part of the moisture now is from external sources, the same evaporation rate is achieved at a larger X (Fig. 2), or conversely, a lower E belongs to the same X than in the linear case of Eq. (6), when such moisture import effects are absent or negligible.

The four BCs however can also be satisfied by a power-function extension of the polynomial solution of Eq. (7), yielding (Szilagyi et al., 2022)

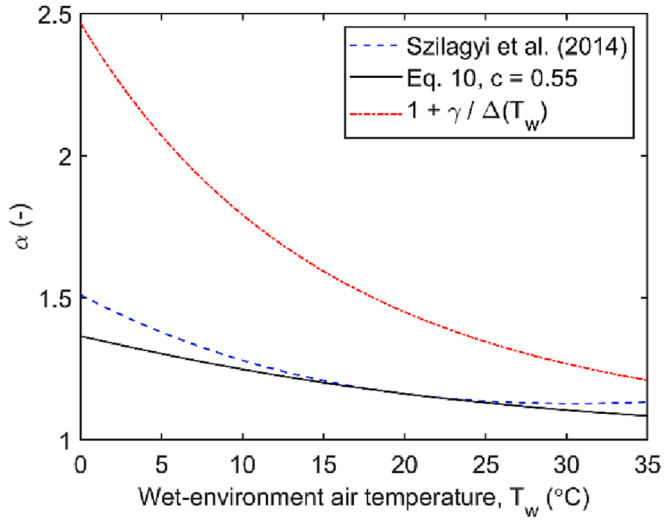

Fig. 4. The Priestley-Taylor coefficient, α, as a function of the wet-environment air temperature (T_w) displayed with its theoretical maximum value (in red) employing standard atmospheric pressure (1000 hPa) in γ. (For interpretation of the references to colour in this figure legend, the reader is referred to the web version of this article.)

$$y = aX^b - (a-1)X^{\frac{ab-1}{a-1}} \quad a, b > 1 \tag{8}$$

where a and b are free parameters. Eq. (7) is recaptured, provided $a \equiv b \equiv 2$. With the $a \equiv 2$ and $b \equiv 1$ choice, Eq. (6) is recovered at the expense of violating BC i). Since $a \equiv 2$ ensures that the new solution can convert back to the existing ones (Eqs. (6) and (7)), the value of a is kept fixed at two from here on, without any discernible loss in practical value, yielding (Szilagyi et al., 2022)

$$y = 2X^b - X^{2b-1} \quad b > 1 \tag{9}$$

Fig. 3 depicts the resulting curves for selected values of b. As the value of b increases, the curves move to the right, get pressed closer to each other to the same increment in the b value, become generally steeper and stay close to zero over longer ranges of X. See Appendix 1 for a demonstration of the effect of external moisture admixing on the shape of the CR curve with actual measurements.

Eq. (9) contains two parameters, α and b, to calibrate. Priestley and Taylor (1972) tentatively set the value of α to be 1.26, a standard value in the majority of applications ever since that employ the Priestley-Taylor equation. Past applications of different, heuristic formulations of the CR (e.g., Brutsaert and Stricker, 1979; Morton, 1983; Kahler and Brutsaert, 2006; Szilagyi, 2015; Han and Tian, 2018; Gao and Xu, 2020) typically assigned values to it (via calibration) from the 1 – 1.32 interval.

2.2. Formulation of a calibration-free CR version

In continental/global-scale applications of the CR (Szilagyi et al., 2017; Ma and Szilagyi, 2019; Ma et al., 2019, 2020, 2021) the temporally and spatially constant value of α was set by the method of Szilagyi et al. (2017) that requires gridded data over a large spatial domain thus, impeding its site-specific, local application. The value of α, however, can be related to the wet-environment air temperature (Andreas et al., 2013; Szilagyi et al., 2014). Andreas et al. (2013) found that the Bowen-ratio, Bo (=H / LE, where H is the sensible while LE the latent heat flux, the latter the evaporation rate multiplied by the latent heat of vaporization, L, employing a water density of 1000 kg m^{-3}), over oceans can be expressed as $Bo = cBo^*$. Here c is a universal constant and Bo^* is the Bowen-ratio of equilibrium evaporation, i.e., when α in Eq. (3) is unity, yielding

$$\alpha = \frac{\Delta(T_w) + \gamma}{\Delta(T_w) + c\gamma} \tag{10}$$

Note that equilibrium profiles of temperature/humidity mentioned later (and frequently observed) do not require equilibrium evaporation, the latter is purely a theoretical term.

Szilagyi et al. (2014) on the other hand expressed α from Eq. (3) employing ERA-Interim (ECMWF, 2007) H and LE reanalysis data over the continents and retained α values whenever the Bo-ratio fell into the theoretically possible [1, 1 + γ / $\Delta(T_a)$] range, assumed to signify wet environmental conditions (i.e., $T_a = T_w$). When plotting those α values against T_w (°C), the third-order best-fit polynomial yielded the following coefficients (in decreasing power order): $-4.84 \bullet 10^{-6}$, $7.07 \bullet 10^{-4}$, $-2.96 \bullet 10^{-2}$, and 1.51. With the c = 0.55 choice in Eq. (10), the two curves overlap (Fig. 4) within the 15 – 25 °C range, the typical mean monthly temperature range of the continents under wet conditions of the warm season when E_w rates are the largest. As Eq. (10) of Andreas et al. (2013) explicitly accounts for altitude (via γ), it should be preferred over the polynomial of Szilagyi et al. (2014).

Note that α in Eq. (10) (similar to the polynomial) does not change much [from 1.13 to 1.2 (with c = 0.55) obtaining 1.16 at 20 °C] within the 15 – 25 °C interval. Below 15 °C, when the change is more pronounced in either curve, a typically reduced value of Q_n is further multiplied by an also reduced value of the Δ (Δ + γ)$^{-1}$ term in Eq. (3), making the difference [i.e., between employing a constant α vs Eq. (10) or the polynomial of Szilagyi et al. (2014)] in the resulting E_w values relatively small in comparison to the warm-season ET rates, the latter values exerting the strongest influence on any parameter calibration results. That is why previous versions of the CR containing a constant but well-chosen α value could still be very successful.

3. Methods

3.1. Description of the FLUXNET data

Monthly and daily meteorological (air pressure, temperature, vapor pressure deficit, and wind speed) data were downloaded from the FLUXNET web site (fluxnet.org) for 171 eddy-covariance stations (listed in Table A2). Latitudes, longitudes, measurement (h_m) and canopy heights (h_c), IGBP land classes (Loveland et al., 2000) were provided for these sites by Wang et al. (2020) and were adopted herein. Separate wind speed, temperature, and humidity measurement heights were not included by Wang et al. (2020), so it is assumed here that they are all measured at the single given height. Net radiation, ground heat conduction, (uncorrected) eddy-covariance sensible and latent heat fluxes were also included in the FLUXNET downloads. All variables employed some gap filling using the MDS [Marginal Distribution Sampling (Reichstein et al., 2005)] method as described by Pastorello et al. (2020). Data flagging, quality assurance and control, and gap-filling for all the variables also followed the procedures outlined by Pastorello et al. (2020).

3.2. Data pre-processing and filtering

Only data for which $H > 0$, $LE > 0$, $Q_n = R_n - G > 0$, and $h_m - h_c > 0$ were further analysed. Because of the wide variance of measurement and canopy heights among the stations, the measured T_a values were transformed into potential temperatures (e.g., Stull, 2000) at the canopy height via $T_p = T_a + g(h_m - h_c) / c_p$, where g is the gravitational acceleration, and the resulting T_p values then used in place of T_a. This step however can be omitted as it has no practically discernible effect on the ensuing ET estimates, unlike the power-function transformation of the wind speed values by $h_m - h_c$ for measurement height, which does have an effect. The variable G was not measured for some of the sites, and missing values of G also occurred. When measurements of G were not

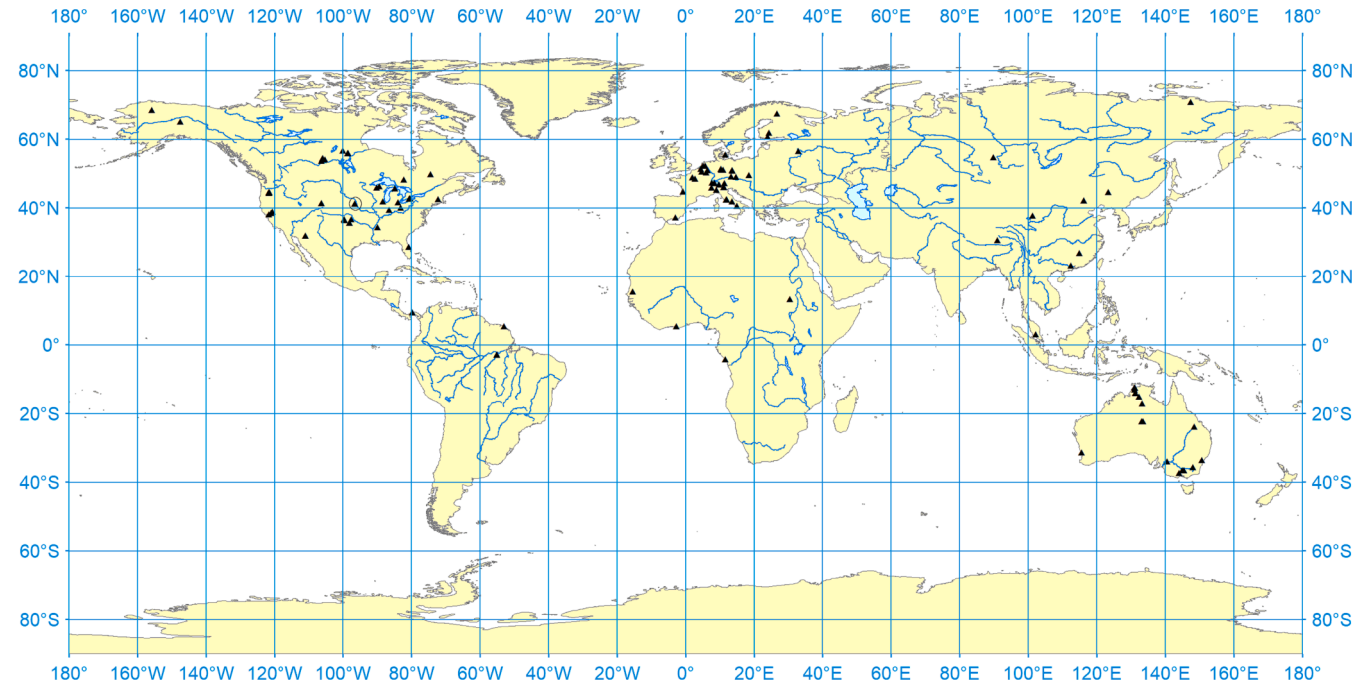

Fig. 5. Global distribution of the 124 FLUXNET stations employed in the data analysis. The Mead, Nebraska (USA) site is circled.

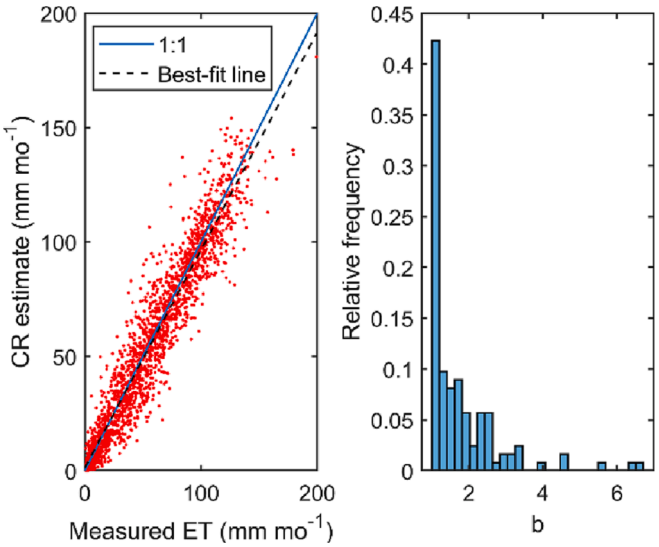

Fig. 6. i) CR-model performance (Table 1) by locally (station-by-station) calibrated α and b values at the 124 FLUXNET stations. ii) Relative histogram of the 124 calibrated b values.

available, a value of zero was assumed. Over a 24-hour period, G is often negligible (Stull, 2000) and it is more so as the averaging time increases.

The FLUXNET dataset includes the variables "H_CORR" and "LE_CORR", which have been corrected to ensure energy budget closure. Issues regarding energy-budget closure techniques with eddy-covariance measurements are complicated, as discussed by Mauder et al. (2020), therefore the use of such data is avoided in this study. Instead, only months where the sum of the uncorrected H and LE ("H_F_MDS" and "LE_F_MDS") values were within 10% of the Q_n value were retained for the ensuing evaluation of the CR. See Table A2 for the stations that had to be excluded because there were fewer than two months meeting this requirement.

At five sites of Table A2 (#43, 44, 47, and 127, all close to the Mediterranean Sea in Italy and #49 at high altitude in the Italian Alps) external moisture admixing is very strong (unrestricted local calibration of α yielding values way below unity), while at an additional three sites (#78, 86, and 92), all near the San Joaquin River delta within the Central Valley of California the opposite, strong dry and hot air transport into the measurement sites (unrestricted local calibration of α yielding values in excess of 1.5) is complicating the general application of the calibration-free CR which accounts for typically moderate moisture admixing and employs $1 < \alpha < 1.36$ (via Eq. (10) and $c = 0.55$) in the warm season of $T_a > 0$ °C. At these sites the CR needs local calibration of at least one (b) of its two parameters, therefore these locations were also excluded, leaving altogether 124 FLUXNET stations (Fig. 5) around the globe to work with. There was one site (#45) with a zero value of $h_m - h_c$, so it also was omitted from further analysis.

Eventually, Eq. (9) with Eq. (10) for the calibration-free case were applied and systematically evaluated for model performance at the 124 FLUXNET stations displayed in Fig. 5.

4. Results

4.1. Local calibration of at least one parameter of the CR model

4.1.1. Simultaneous local calibration of α and b

Station-by-station (i.e., local) calibration of α and b in Eq. (9) yielded the best model performance (Fig. 6, Table 1) with a root-mean-square error (RMSE) of about 12 mm mo^{-1}, Nash-Sutcliffe Efficiency (NSE) of 91% and explained variance (R^2) of also 91%. Relative bias is less than 3% and the best-fit line has a slope of 0.95. At about 42% of the stations the calibrated value of b is unity or very close to it (Fig. 6), suggesting that external moisture admixing into the daytime developing boundary layer often exerts only a negligible effect on the resulting ET rates during drying of the environment. This effect is naturally negligible in humid environments where soil moisture status rarely drops below its field capacity value due to frequent and abundant precipitation events. However, at the remaining (58%) sites, such effects are significant, yielding a mean b value of 1.75. The 1.15 average of the calibrated α values is very close to what Eq. (10) (with $c = 0.55$) provides (i.e., 1.16) at 20 °C (Fig. 4).

Table 1
Performance statistics of Eq. (9) with different parameter-calibration choices, as well as that of Morton's calibration-free WREVAP model. R: linear correlation coefficient between measured and estimated ET values; R^2: explained variance; RMSE: root-mean-squared-error; RB: relative bias; MAE: mean absolute error; NSE: Nash-Sutcliffe model efficiency; RS: ratio of standard deviations of the modeled and measured ET values; x_{50}, $\langle x \rangle$: median and mean of the specified variable, x; x_{opt}: globally calibrated value of the specified parameter. Q_n^* is available energy at the surface estimated by Morton's WREVAP program from global (i.e., incoming solar) radiation measurements. Systematic trial-and-error calibration of α and b took place within the 1 – 1.32 and 1 – 10 intervals, respectively. In each class of models, the best performance-measure value is boldened.

Local calibration of at least one parameter	R	R^2 (%)	RMSE (mm/mo)	RB	MAE (mm/mo)	NSE (%)	RS	Best-fit slope
Fig. 6								
$\alpha_{50} = 1.15$ $\langle\alpha\rangle = 1.15$ $b_{50} = 1.4$ $\langle b\rangle = 1.75$	**0.953**	**90.91**	**11.61**	−0.027	**8.612**	**90.53**	**0.999**	0.953
Fig. 7								
$\alpha = f(T_w)$ $b_{50} = 1.9$ $\langle b\rangle = 2.3$	0.934	87.17	13.86	**−0.005**	10.57	86.5	1.016	0.949
Fig. 9								
$\alpha_{opt} = 1.12$ $b_{50} = 1.4$ $\langle b\rangle = 1.76$	0.934	87.3	13.82	−0.039	10.44	86.58	0.993	0.928
Fig. 10								
$\alpha_{50} = 1.18$, $\langle\alpha\rangle = 1.18$, $b \equiv 2$	0.941	88.64	13.53	−0.048	10.22	87.13	1.038	**0.977**
$\alpha_{50} = 1.08$, $\langle\alpha\rangle = 1.11$, $b \equiv 1$	0.934	87.16	13.55	0.015	10.08	87.08	0.95	0.887
Global calibration of at least one parameter								
Fig. 11								
$\alpha_{opt} = 1.09$ $b_{opt} = 1.4$	**0.904**	**81.67**	**16.4**	−0.027	**12.47**	**81.09**	**0.968**	0.875
$\alpha = f(T_w)$ $b_{opt} = 1.8$	0.9	81	17.47	0.032	13.3	78.54	1.049	0.944
Fig. 12								
$\alpha_{opt} = 1.15$ $b \equiv 2$	0.902	81.28	18.06	−0.053	13.94	77.07	1.089	**0.982**
$\alpha_{opt} = 1.07$ $b \equiv 1$	0.899	80.74	16.59	**−0.007**	12.53	80.65	0.926	0.832
No calibration								
$\alpha = f(T_w)$ $b \equiv 2$ (with Q_n^*)	0.87	75.76	20.88	−0.054	15.94	69.34	1.11	**0.966**
$\alpha = f(T_w)$ $b \equiv 2$ ($u_2 \equiv 2$ m/s)	0.893	79.74	17.78	−0.003	**13.63**	77.77	1.035	0.924
$\alpha = f(T_w)$ $b \equiv 2$ (with Q_n^*, $u_2 \equiv 2$ m/s)	0.864	74.73	21.06	−0.049	16.01	68.8	1.096	0.947
Fig. 13								
$\alpha = f(T_w)$ $b \equiv 2$	**0.896**	**80.37**	**17.76**	−0.007	13.66	**77.82**	1.056	0.946
$\alpha = f(T_w)$ $b \equiv 1$	0.896	80.28	19.36	0.147	14.56	73.63	**1.013**	0.907
Morton's WREVAP	0.843	71.13	25.36	**0.001**	18.79	54.76	1.248	1.052

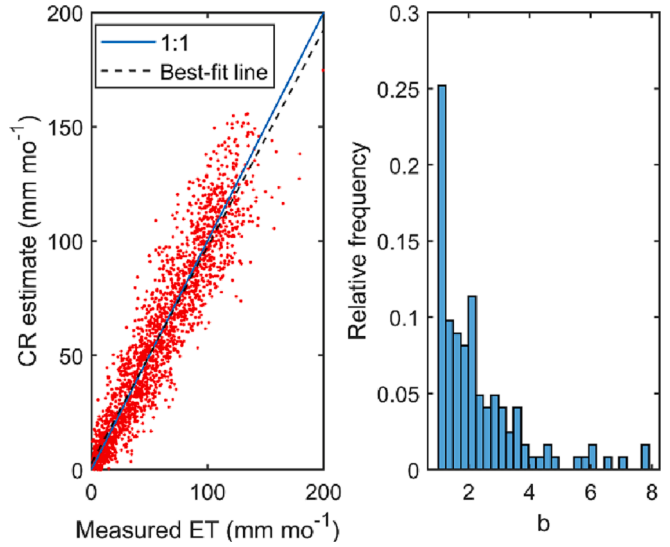

Fig. 7. i) CR-model performance (Table 1) via locally calibrated b values at the 124 FLUXNET stations. α is provided by Eq. (10) ($c = 0.55$). ii) Relative histogram of the 124 calibrated b values.

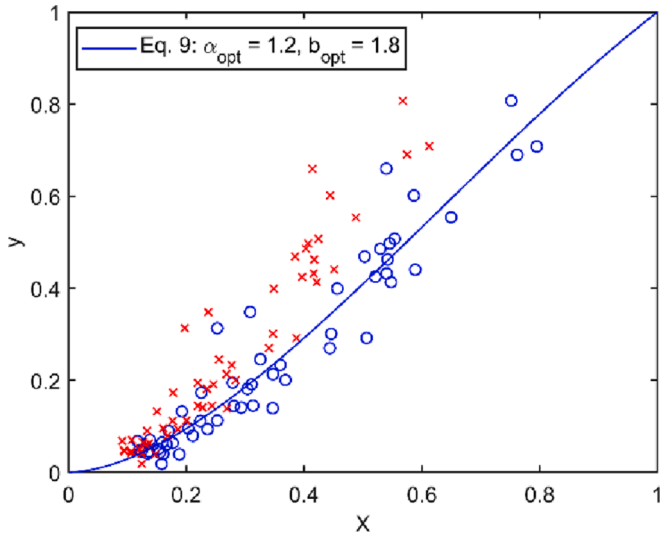

Fig. 8. Eq. (9), calibrated for station #3 in Table A2. The blue circles represent the non-dimensional values of the measurements when $\alpha_{opt} = 1.2$ in X, while the red marks when $\alpha = 1$, set here arbitrarily. (For interpretation of the references to colour in this figure legend, the reader is referred to the web version of this article.)

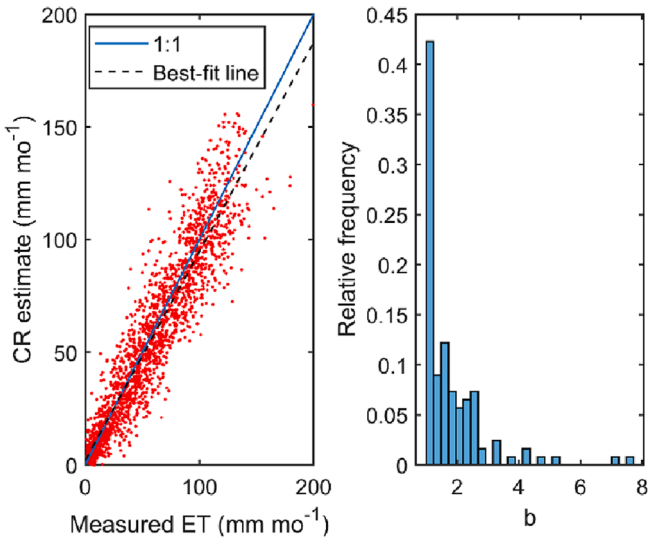

Fig. 9. i) CR-model performance (Table 1) by globally (all-stations-at-once) calibrated α ($\alpha_{opt} = 1.12$), and locally calibrated b values at the 124 FLUXNET stations. ii) Relative histogram of the 124 calibrated b values.

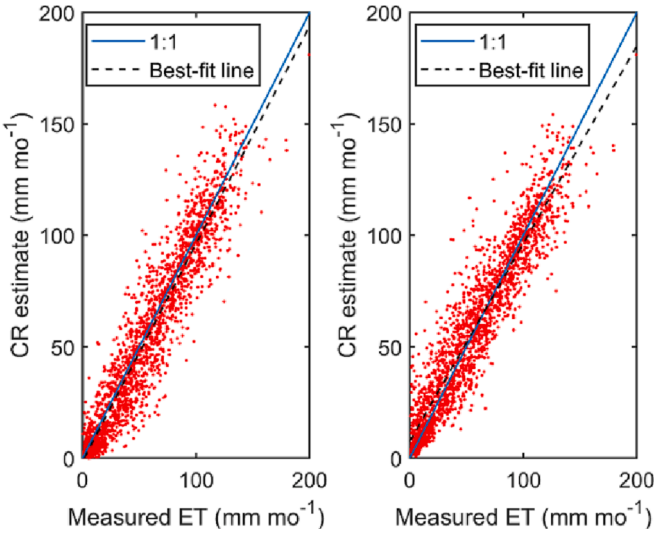

Fig. 10. CR-model performance (Table 1) by locally calibrated α at the 124 FLUXNET stations. i) $b \equiv 2$; ii) $b \equiv 1$.

4.1.2. Calibration of b only

By setting the α values via Eq. (10) ($c = 0.55$), the single-parameter CR model still performs well (Fig. 7, Table 1: RMSE of about 14 mm mo^{-1}, NSE of 86%, and R^2 of 87%) having practically no bias at all and retaining a best-fit slope of 0.95. This time, however, at only about 25% of the stations can one find negligible effects of external moisture admixing on the resulting ET rates, while at around two, the histogram of the b values displays a secondary mode, with a median of 1.9 and mean of 2.3. This indicates that the existing polynomial model (Eq. (9) with $b \equiv 2$) of Szilagyi et al. (2017) describes the effect of moisture admixing on the resulting ET rates properly in an average sense, evidenced by the mode, median and mean values of b, all being close to two.

When α is treated as a free parameter, as for Fig. 6, it will move the measured values horizontally in the non-dimensional graph of y vs X (Fig. 8). Note that the curve of Eq. (9) remains fixed, independent of the

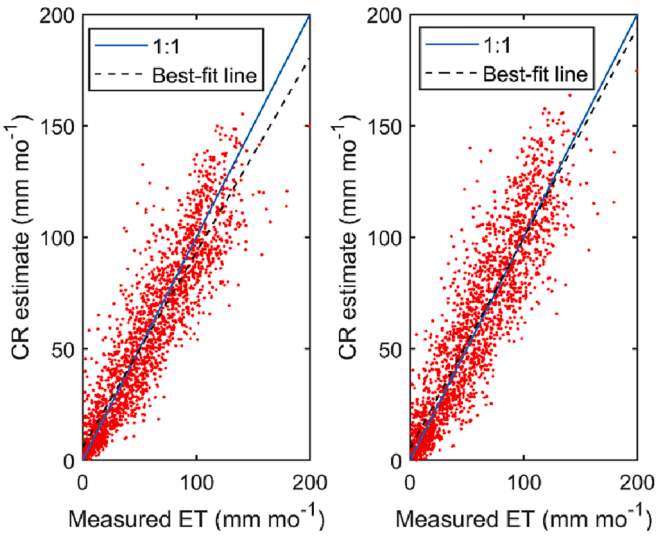

Fig. 11. CR-model performance (Table 1) via global (all stations at once) calibration. i) $\alpha_{opt} = 1.09$ and $b_{opt} = 1.4$; ii) α from Eq. (10) with $c = 0.55$, and $b_{opt} = 1.8$.

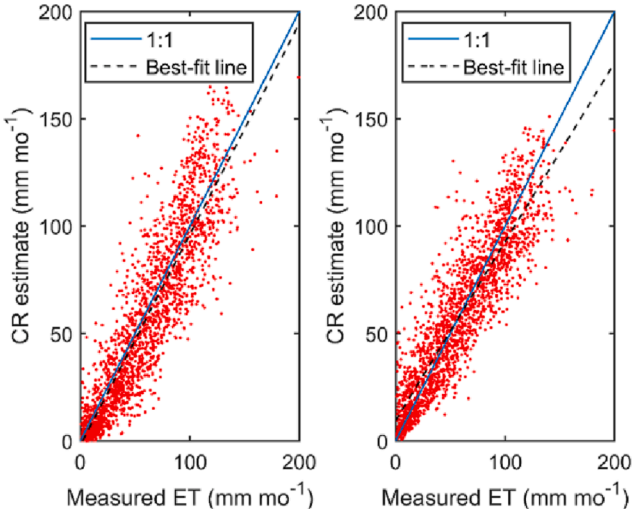

Fig. 12. CR-model performance (Table 1) via globally calibrated α. i) $\alpha_{opt} = 1.15$, $b \equiv 2$; ii) $\alpha_{opt} = 1.07$, $b \equiv 1$.

value of α, but rather the measurement points when placed on the graph move horizontally according to the actual value of α. The larger its value the more the measurement points move to the right on the X axis, and vice-versa, for declining α values the measurement points move to the left. The measurement points, however, do not move by the same extent: the y values at larger X move horizontally farther than points found at smaller values of X. So in this way, α acts in a manner complementary to b. While b changes the general slope of the curve of Eq. (9) (on top of moving the curve horizontally as well) to fit the measurements, α changes the slope along which the measurement points align in the non-dimensional graph, and doing so affects the calibration of b. This is the reason why the number of cases with negligible effects of external moisture admixing is different between Figs. 6 and 7. Since Eq. (10) derives the α values independently of b or the CR in general, it is believed that Fig. 7ii represents the distribution of the shape parameter value and therefore the number of stations where external moisture

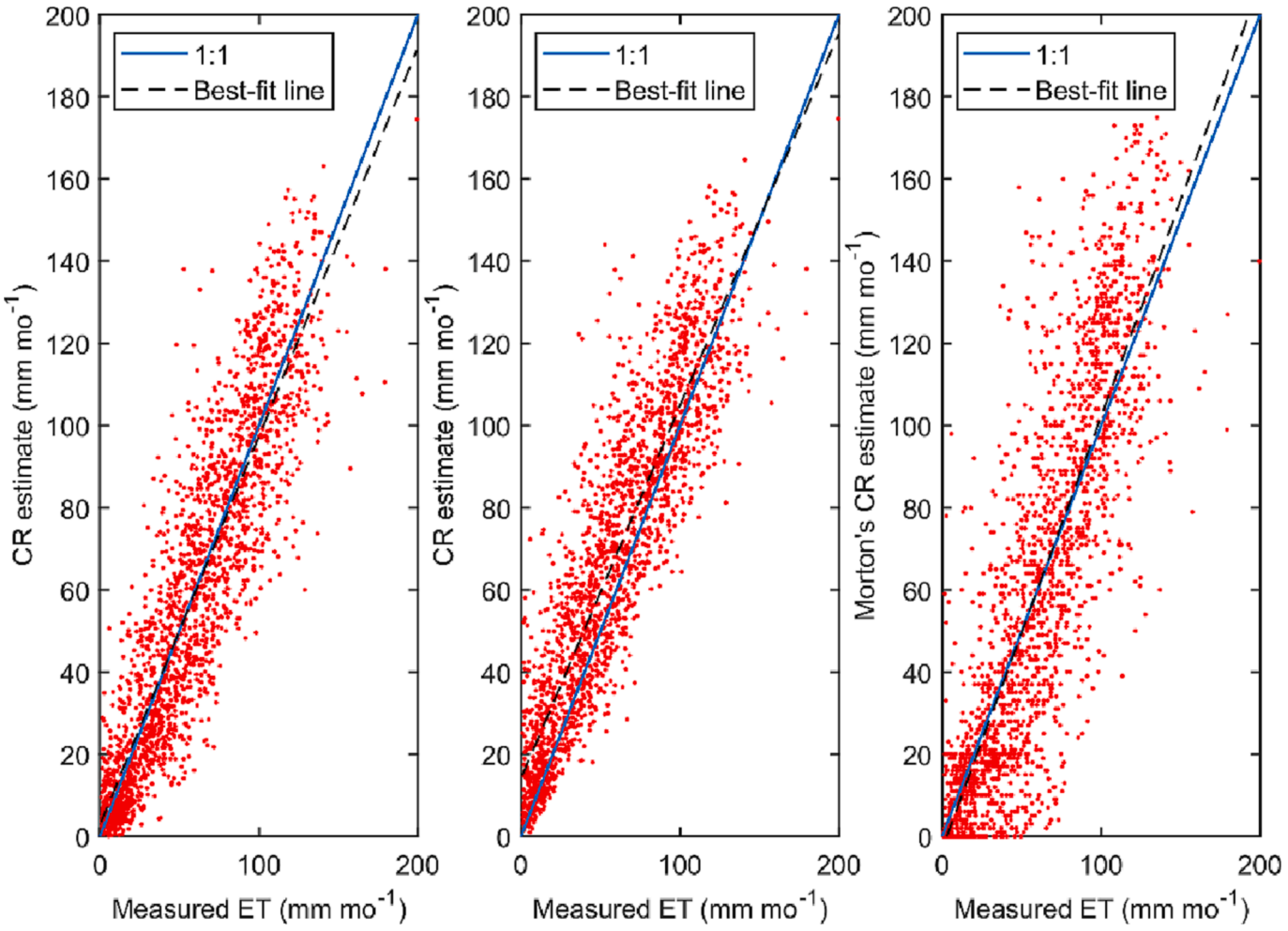

Fig. 13. Performance (Table 1) of the calibration-free CR model via α specified by Eq. (10) with the $c = 0.55$ choice for i) $b \equiv 2$, and; ii) $b \equiv 1$. In comparison, performance of Morton's CR-based calibration-free WREVAP model is also included in iii).

admixing is negligible better than Fig. 6ii. This statement is corroborated below through the outstanding performance of the polynomial version of the CR that employs a b value of two.

4.1.3. Global calibration of α and local calibration of b

The value of α can also be set globally, by calibrating it against all stations at once. Interestingly, the calibrated value of 1.12 is exactly the same as Szilagyi et al. (2017) obtained for Eq. (7), employing water-balance data of 334 watersheds covering fully the conterminous US. The resulting model performance (Fig. 9 and Table 1) is very close to the previous one that employs Eq. (10) for α.

4.1.4. Calibration of α with prescribed values of b

As seen so far from the histograms (Figs. 6, 7, and 9), the calibrated value of b stays predominantly (>95% of the cases) within the 1 - 4 interval, with a mean value of about two, and having a value of unity as the most frequently calibrated single value. Both observations warrant further investigation of these two, already existing versions of the CR, i.e., when $b \equiv 1$ (linear form of Crago et al., 2016) and when $b \equiv 2$ (polynomial version of Szilagyi et al., 2017). As discussed above, the $b \equiv 1$ case represents negligible external moisture effects on the resulting ET rates, while the $b \equiv 2$ case an average (moderate) one. Fig. 10 displays the resulting model performance for each case.

Model performance (Table 1) is more-or-less similar to the previous two cases, however, the polynomial form (i.e., $b \equiv 2$) of Eq. (9) explains best the variance of the EC measurements with R^2 of 89%, RMSE of 14 mm mo^{-1}, and NSE of 87% of all one- or globally calibrated two-parameter cases investigated in this study, with a calibrated α (median and mean 1.18) closest to the Priestley and Taylor (1972) value of 1.26, and a best-fit slope (0.98) very close to unity. The linear version ($b \equiv 1$), having a median and mean of the calibrated α values as 1.08 and 1.11, respectively, is better than the polynomial one only in its relative bias and mean absolute error statistics. As discussed previously, the average (and median) calibrated value of α has to be lower in the linear case in order to move the measurement points to the left since the linear 'curve' is the farthest to the left in Fig. 3. The polynomial model which attains calibrated α values closer to the Priestley and Taylor (1972) obtained value of 1.26 and also from within the range of 1.13 – 1.2 in Fig. 4 for T_w values within 15 – 25 °C, plus yields a best-fit slope closer to unity [and corresponding intercept value (Fig. 10) close to zero] should definitely be preferred, even without mentioning the better R^2, RMSE and NSE statistics.

4.2. Global calibration of at least one parameter of the CR model

4.2.1. Simultaneous calibration of α and b

As expected, a move from local to global calibration yields a decrease in model efficiency. When both parameters of Eq. (9) are globally calibrated (Fig. 11i), the RMSE value increases to 16 mm mo^{-1}, NSE drops to 81%, and the best-fit slope also suffers (0.87).

4.2.2. Calibration of b only

When α is expressed by Eq. (10), RMSE increases a bit, to 17 mm mo^{-1}, NSE drops slightly to 79%, while the best-fit slope significantly improves to 0.94 (Fig. 11ii).

4.2.3. Calibration of α with prescribed values of b

From the two cases when the value of b is set and α is calibrated globally (Fig. 12), the linear version ($b \equiv 1$) practically maintains the performance (Table 1) of the two-parameter case in Fig. 11i, on the expense of a further degrading best-fit slope value (0.83).

4.3. The calibration-free CR model

Finally, the calibration-free polynomial (i.e., $b \equiv 2$) version of Eq. (9) (Fig. 13i) has an RMSE of about 18 mm mo^{-1}, NSE of 78%, and a best-fit slope of 0.95. It is only slightly weaker in performance (Table 1) than the globally calibrated (for α) linear version in Fig. 12ii or the globally calibrated two-parameter one in Fig. 11i, while it is slightly better than its globally calibrated version in Fig. 12i. While the calibration-free linear version is the weakest of all versions of Eq. (9) tested, all tested versions of Eq. (9) in fact perform better than Morton's calibration-free WREVAP model.

As seen, the calibration-free model results improve significantly upon Morton's WREVAP model (Morton et al., 1985), the only other available calibration-free CR-based ET estimation method, requiring even fewer input data than the current CR version, as it does not need wind measurements and estimates Q_n from more widely available measurements of solar radiation. The current calibration-free CR version still works better than WREVAP, even when wind data is replaced by a constant 2 m s^{-1} value, as a general substitute for such measurements and/or when available energy at the surface is estimated from solar radiation measurements (Table 1) by the method of Morton et al. (1985). The reason for this improvement lies chiefly in the fact that Morton (1983) assumed the CR to be symmetric (i.e., $E_w - E = E_p - E$), which since has been empirically proven to be incorrect in general (Kahler and Brutsaert, 2006; Brutsaert, 2015), and most recently, from thermodynamical considerations (Crago and Qualls, 2021; Szilagyi, 2021) as well, even though there are examples when the CR is close to a symmetric form (Huntington et al., 2011; Ma et al., 2015).

5. Summary and conclusions

The present study aimed to systematically demonstrate the capability of a recently derived simple complementary-relationship-based evapotranspiration estimation method (Szilagyi et al., 2022) that requires a minimum number of input variables only, and versatile in its structure (with an optional number of parameters to calibrate between zero and two) to allow for its calibration-free application. The calibration-free formulation of this CR method (i.e., expressing α with Eq. (10)) has never been published nor evaluated before.

The thermodynamics-based CR equation (i.e., Eq. (9)) was tested with monthly data of 124 FLUXNET stations around the globe to see how the i) number of calibrated parameters; ii) type of calibration (local and/or global), and; iii) nature of the relationship [i.e., whether it is linear ($b \equiv 1$), polynomial ($b \equiv 2$), or in the form of a power-function] between the nondimensional variables affect the estimation results.

The locally calibrated two-parameter (power-function) CR version (Szilagyi et al., 2022) performed the best. It was followed by the locally calibrated, single-parameter (α), polynomial CR version of Szilagyi et al. (2017), outperforming all other single- or globally calibrated two-parameter versions. In the calibration-free category, again the polynomial version outperformed the linear one (Crago et al., 2016), even when a constant wind speed was used in the former. The success of the polynomial version of Eq. (9) must lie in its ability of efficiently accounting for the average effect of external moisture admixing on the resulting drying-environment ET rates, and by doing so making a universal, calibration-free CR version formulation possible where the remaining parameter (α) of Eq. (9) is derived from both physical (as a function of the wet-environment air temperature in Eq. (10)) as well as empirical considerations (the concrete value of c in Eq. (10)).

The novel, calibration-free CR can be employed in situations where local calibration is unfeasible due to lack of measured flux or water-balance component data, provided external moisture admixing is not too extreme, such as found near Mediterranean (in the summer), semi-desert (e.g., in southern California) or desert (e.g., in Peru or Namibia) coastlines where the moisture content of the air, arriving from over the sea can be strongly decoupled from the moisture status of the dry/semi-dry land. It outperforms the only existing other calibration-free ET-estimation method of Morton's (1985) WREVAP code even when wind data is replaced by a constant value of 2 m s^{-1} (to bring it on an even footing with the latter which does not require wind measurements) and Q_n is replaced by the WREVAP code's estimate, derived from global radiation data.

Where calibration is feasible, the two- or single-parameter ($b \equiv 2$) versions of Eq. (9) are recommended.

Even the existing, single-parameter, polynomial version (Szilagyi et al., 2017) of Eq. (9), with the spatially constant value of α set globally by the procedure described in Szilagyi et al. (2017) have been shown on a continental/global scale (Szilagyi, 2018; Ma and Szilagyi, 2019; Ma et al., 2019, 2020, 2021) to outperform or match often complex, and data intensive, large-scale evaporation estimation methods (several of them employed in the land surface model components of different widely used global climate models). The two-parameter version has also been demonstrated to outperform (Szilagyi et al., 2022) other CR-based two-parameter methods.

This success can only occur because Eq. (9) is built on atmospheric thermodynamics as opposed to largely heuristic approaches of other ET estimation techniques whether they are based on earlier formulations of the CR or not.

Any CR formulation in general, is based on an acquired equilibrium state between the land and the overlying atmosphere. As such takes time to develop (Morton, 1983), the CR is not recommended to be applied routinely with time steps shorter than five days to a week. In fact, it has already been shown (Crago et al., 2022) that the CR works best on a monthly basis, ideal for most water resources applications/investigations.

Further studies are required to relate the value of b to some large-scale measure of wetness-contrast in space. Distance to sea/lake shores upstream of the prevailing wind combined with an appropriate aridity measure of the site might be one such metric that could also identify locations where either the calibration-free version [due to a necessary large b ($\gg 2$) value requirement] or the CR itself (due to $b >$ 10) should not be recommended.

A crucial original insight by Bouchet (1963) about the complementary nature of concurrent actual and potential ET rates, with the pioneering work of Brutsaert and Stricker (1979), Morton (1983), as well as further inspiring ideas by Brutsaert (2015), with additional inputs from Szilagyi and Jozsa (2008), Andreas et al. (2013), Szilagyi et al. (2014), Crago et al. (2016), Szilagyi et al. (2017), Crago and Qualls (2021), Szilagyi (2021), and Szilagyi et al. (2022) have led to the present thermodynamics-based, calibration-free version of the CR, formulated by Eqs. (9) and (10). Its two parameters, α and b, have clear physical meaning as well. While α accounts for the free tropospheric air entrainment (e.g., Lhomme, 1997a, b) into the daytime developing convective boundary layer during wet-environmental conditions, b does the same for moisture admixing during drying conditions. When

calibration is feasible and required, it can easily be performed with values taken from the 1 – 1.32 and 1 – 10 intervals for α and b, respectively.

It is hoped that Eq. (9) with its minimal data requirement and versatility will be employed and further tested during this period of climate change for better future management and (re)allocations of existing water resources.

Declaration of Competing Interest

The authors declare that they have no known competing financial interests or personal relationships that could have appeared to influence the work reported in this paper.

Data availability

Data will be made available on request.

Acknowledgments

The authors are grateful for the two anonymous reviewers whose comments led to important changes in the original text. Support provided by the i) Ministry of Innovation and Technology of Hungary from the National Research, Development and Innovation Fund, financed under the TKP2021-NVA funding scheme (project# TKP-6-6/PALY-2021), and; ii) Szechenyi Plan Plus program (project# RRF-2.3.1-21-2022-00008) is kindly acknowledged.

Appendix 1

At the Mead, Nebraska (USA) FLUXNET stations (circled in Fig. 5) the deficit-irrigated maize (corn) site is close to the non-irrigated (rainfed) one of maize/soybean rotation (maize in one year, soybean the other). Mean monthly ET for the warm months with mean air temperature in excess of 10 °C is 75 mm mo^{-1} at the irrigated site, while at the rainfed site it is 71 mm mo^{-1}. Both sites are near the south-eastern edge of the large, irrigated corn region of Nebraska. When Eq. (9) is calibrated separately for the two sites, the b value (b_{opt}) becomes 1.8 for the rainfed site, and 1.6 for the irrigated one (Fig. A1). The larger value of b for the drier, rainfed site is likely caused by the enhanced influence of external moisture admixing from the neighboring wetter irrigated fields, relative to what the irrigated FLUXNET site experiences.

To further illustrate the effect of external moisture import on the value of parameter b in Eq. (9), the months were separated into two groups: a) when the difference in irrigated and rainfed ET rates is larger than their average (30 such months) difference, and; b) when it is lower (the remaining 30 months). In this latter case, when both fields are similarly wet, there is no difference in the effect of moisture admixing on the resulting calibrated curves, as seen in Fig. A2.

However, the effect of external moisture-import diverges when the difference in ET rates between the more moist irrigated and the drier rainfed field is amplified (Fig. A3), the former being less influenced by such external moisture admixing, reflected in the reduced value of b_{opt}.

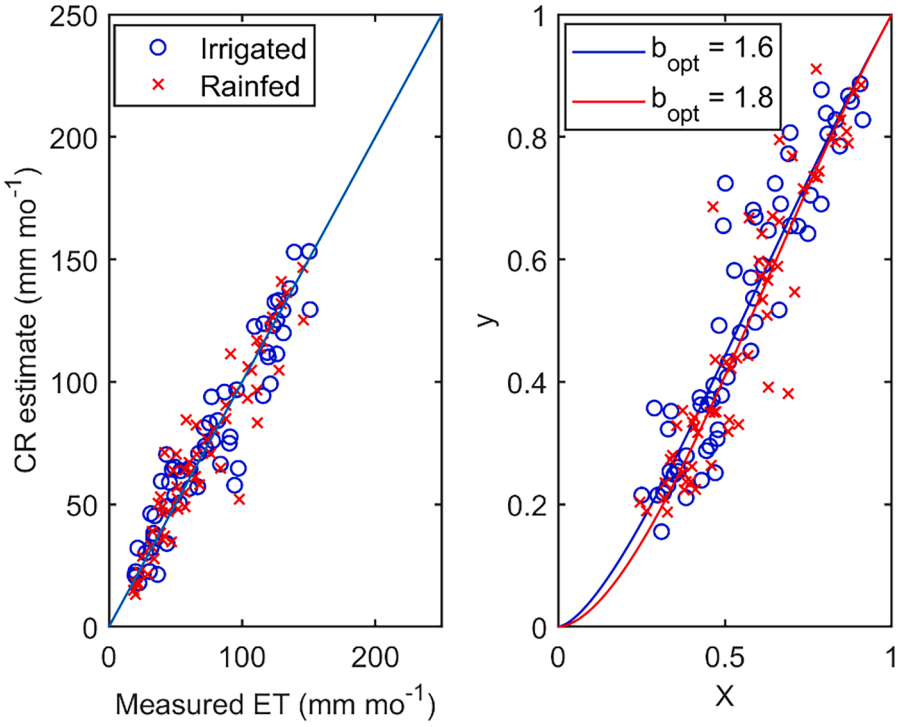

Fig. A1. Measured and Eq. (9) estimated monthly ET rates at two FLUXNET stations, one irrigated, one rainfed (#63 and 90 in Table A2) near Mead, Nebraska (USA). In panel ii) (right one) the curves represent Eq. (9) for the two calibrated, b_{opt}, values. The CR estimates in panel i) result from Eq. (9) multiplied by the corresponding monthly E_p rate of Eq. (2).

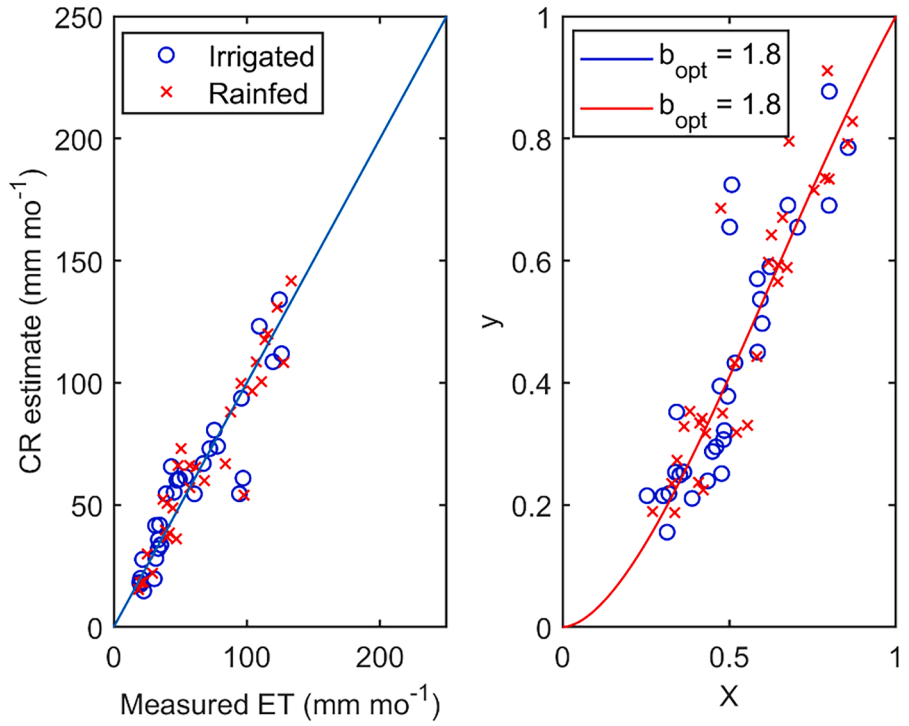

Fig. A2. Same as Fig. A1 except for months with smaller than average difference in irrigated and rainfed ET rates.

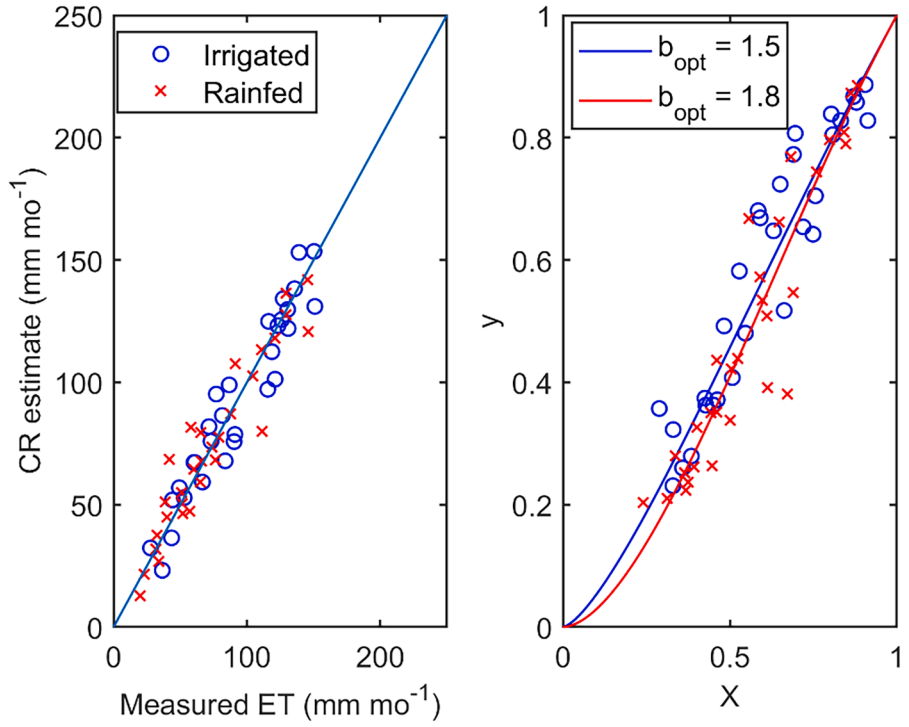

Fig. A3. Same as Fig. A1 except for months with larger than average difference in irrigated and rainfed ET rates.

Appendix 2

Table A2
List of the 171 FLUXNET sites considered for CR model application. Stations marked with an Asterix were left out of the application of the CR because energy closure error in the measured fluxes was>10% for each available month of that station.

	Site	Lat	Lon	Measurement Height (m)	Canopy Height (m)	IGBP Class
1	AU-How	−12.494	131.152	23	15	WSA
2	AU-Rig	−36.65	145.576	5	0.4	GRA
3	AU-Stp	−17.151	133.35	4.2	0.2	GRA
4	AU-Tum	−35.657	148.152	70	40	EBF
5	AU-Wac*	−37.426	145.188	95	70	EBF
6	AU-Whr	−36.673	145.029	35	28	EBF
7	AU-Wom	−37.422	144.094	29	25	EBF
8	AU-Ync*	−34.989	146.291	20	0.5	GRA
9	BE-Lon	50.552	4.746	2.7	0.5	CRO
10	BR-Sa3	−3.018	−54.971	64	27	EBF
11	CA-Qfo	49.693	−74.342	24	13.8	ENF
12	CA-SF1	54.485	−105.818	12	6	ENF
13	CA-SF2	54.254	−105.878	10	4	ENF
14	AT-Neu	47.117	11.318	2	0.76	GRA
15	AU-ASM	−22.283	133.249	11.7	6.5	ENF
16	AU-Cpr	−34.002	140.589	20	5	SAV
17	AU-DaP	−14.063	131.318	18	0.5	GRA
18	AU-DaS	−14.159	131.388	20.4	16.4	SAV
19	AU-Dry	−15.259	132.371	16.3	12.3	SAV
20	AU-Emr	−23.859	148.475	6.7	0.4	GRA
21	AU-Gin	−31.376	115.714	15	6.8	WSA
22	CH-Cha	47.21	8.41	2	0.5	GRA
23	CH-Dav	46.815	9.856	35	18	ENF
24	CH-Fru	47.116	8.538	2	0.5	GRA
25	CN-Cng	44.593	123.509	6	0.5	GRA
26	DE-Geb	51.1	10.914	6	1	CRO
27	DE-Gri*	50.95	13.513	3	0.5	GRA
28	DE-Hai	51.079	10.453	43.5	33	DBF
29	DE-Lkb	49.1	13.305	9	0.4	ENF
30	DE-Obe	50.787	13.721	42	13.5	ENF
31	DE-She	50.871	6.45	2	0.5	CRO
32	DE-Tha	50.962	13.565	42	30	ENF
33	DK-Sor	55.486	11.645	57	25	DBF
34	FI-Hyy	61.847	24.295	67.2	15	ENF
35	FI-Jok*	60.899	23.513	3	0.2	CRO
36	FI-Sod	67.362	26.639	23	12.7	ENF
37	FR-Gri	48.844	1.952	2.8	2	CRO
38	FR-LBr	44.717	−0.769	25	18	ENF
39	IT-CA1	42.38	12.027	5	1	DBF
40	IT-CA2	42.377	12.026	5	0.5	CRO
41	IT-CA3	42.38	12.022	5	1	DBF
42	IT-Col	41.849	13.588	25.2	20.2	DBF
43	IT-Cp2	41.704	12.357	15	12	EBF
44	IT-Cpz	41.705	12.376	15	12	EBF
45	IT-Lav	45.956	11.281	28	28	ENF
46	IT-MBo	46.015	11.046	2.5	0.3	GRA
47	IT-NOE	40.606	8.151	2	1.75	CSH
48	IT-PT1	45.201	9.061	33	26.6	DBF
49	IT-Ren	46.587	11.434	41	31	ENF
50	IT-SRo*	43.728	10.284	23.5	18	ENF
51	IT-Tor	45.844	7.578	2.5	0.5	GRA
52	NL-Loo	52.167	5.744	52	15.9	ENF
53	RU-Ha1	54.725	90.002	2.5	0.5	GRA
54	SD-Dem	13.283	30.478	9	5	SAV
55	US-AR1	36.427	−99.42	4	1	GRA
56	US-AR2	36.636	−99.598	4	1	GRA
57	US-ARM	36.606	−97.489	60	0.5	CRO
58	US-Blo	38.895	−120.633	8.5	4	ENF
59	US-GLE	41.367	−106.24	22.65	18	ENF
60	US-KS2	28.609	−80.672	4.1	2	CSH
61	US-Me2	44.452	−121.557	32	16	ENF
62	US-MMS	39.323	−86.413	46	27	DBF
63	US-Ne1	41.165	−96.477	6.2	2	CRO
64	US-Ne2	41.165	−96.47	6.2	2	CRO
65	US-Syv	46.242	−89.348	36	27	MF
66	US-Wi9*	46.619	−91.081	9	2.3	ENF
67	US-Wi8*	46.722	−91.252	3	1.5	DBF
68	US-Wi7*	46.649	−91.069	3	0.5	OSH
69	US-Wi6*	46.625	−91.298	3	0.5	OSH
70	US-Var	38.413	−120.951	2	0.3	GRA
71	US-Wi5*	46.653	−91.086	6	4	ENF

(*continued on next page*)

Table A2 (*continued*)

	Site	Lat	Lon	Measurement Height (m)	Canopy Height (m)	IGBP Class
72	US-Wi4*	46.739	−91.166	23	18	ENF
73	US-Wi3*	46.635	−91.099	26	21	DBF
74	US-WCr	45.806	−90.08	29.6	24	DBF
75	US-Wi2*	46.687	−91.153	9	6	ENF
76	US-Wi1*	46.73	−91.233	9	6	DBF
77	US-UMd	45.563	−84.698	34	22	DBF
78	US-Twt	38.109	−121.653	3.15	0.5	CRO
79	US-UMB	45.56	−84.714	46	22	DBF
80	US-Ton	38.432	−120.966	23	9.41	WSA
81	US-Tw3	38.116	−121.647	2.8	0.5	CRO
82	US-Tw4*	38.103	−121.641	3.7	0.1	WET
83	US-Tw2*	38.105	−121.643	5.15	2	CRO
84	US-SRG	31.789	−110.828	8	2.5	GRA
85	US-SRM	31.821	−110.866	6.4	2.5	WSA
86	US-Tw1	38.107	−121.647	4.64	0.1	WET
87	US-SRC*	31.908	−110.84	4.25	1.7	MF
88	US-Oho	41.555	−83.844	32	20	DBF
89	US-Prr	65.124	−147.488	11	2.44	ENF
90	US-Ne3	41.18	−96.44	6.2	2	CRO
91	US-ORv	40.02	−83.018	9.6	0.5	WET
92	US-Myb	38.05	−121.765	4.6	0.5	WET
93	US-Me6*	44.323	−121.608	12	5.2	ENF
94	US-Me3	44.315	−121.608	12	3.1	ENF
95	US-Me5*	44.437	−121.567	20	4	ENF
96	US-Me4	44.499	−121.622	47	33	ENF
97	US-LWW*	34.96	−97.979	3	0.6	GRA
98	US-Me1	44.579	−121.5	47	33	ENF
99	US-Ha1	42.538	−72.172	30	26	DBF
100	US-IB2	41.841	−88.241	3.76	0.5	GRA
101	US-Ivo	68.487	−155.75	3	0.5	WET
102	US-Goo	34.255	−89.874	4	0.3	GRA
103	RU-Fyo	56.462	32.922	42.8	34.8	ENF
104	US-CRT*	41.628	−83.347	2	1	CRO
105	US-Atq*	70.47	−157.409	2.5	0.5	WET
106	US-GBT	41.366	−106.24	29	1	ENF
107	US-Arc	35.546	−98.04	4	0.5	GRA
108	SN-Dhr	15.403	−15.432	9	3	SAV
109	RU-Cok	70.829	147.494	4.7	0.3	OSH
110	US-Arb	35.55	−98.04	4	0.5	GRA
111	NL-Hor	52.24	5.071	4.3	0.5	GRA
112	PA-SPs	9.314	−79.631	3	0.09	GRA
113	PA-SPn	9.318	−79.635	15	10	DBF
114	MY-PSO	2.973	102.306	52	35	EBF
115	IT-Ro2	42.39	11.921	18.6	17	DBF
116	IT-Ro1	42.408	11.93	18.6	17	DBF
117	IT-SR2*	43.732	10.291	23.5	18	ENF
118	IT-BCi	40.524	14.957	3.8	0.3	CRO
119	FR-Pue*	43.741	3.596	11	6	EBF
120	IT-La2	45.954	11.285	33	30	ENF
121	IT-Isp*	45.813	8.634	24	19	DBF
122	GF-Guy	5.279	−52.925	52	32	EBF
123	FR-Fon	48.476	2.78	35	25	DBF
124	GH-Ank	5.269	−2.694	65	30	EBF
125	FI-Lom*	67.997	24.209	3	0.1	WET
126	FI-Let	60.642	23.96	2.75	0.1	ENF
127	ES-Amo	36.834	−2.252	3.05	0.3	OSH
128	ES-LgS	37.098	−2.966	2.25	0.2	OSH
129	DK-Fou*	56.484	9.587	3.5	2	CRO
130	DE-RuS	50.866	6.447	2.2	2	CRO
131	DE-Zrk*	53.876	12.889	2.63	0.1	WET
132	DE-SfN*	47.806	11.328	6	2	WET
133	DE-RuR*	50.622	6.304	2.6	0.1	GRA
134	DE-Lnf	51.328	10.368	44	34	DBF
135	CZ-wet	49.025	14.77	2.7	0.1	WET
136	CZ-BK1	49.502	18.537	15	9.5	ENF
137	CN-Qia	26.741	115.058	39	12	ENF
138	CN-Sw2*	41.79	111.897	2	0.5	GRA
139	CN-HaM*	37.37	101.18	2.5	0.2	GRA
140	CN-Ha2	37.609	101.327	2.5	0.55	WET
141	CN-Du3	42.055	116.281	4	0.2	GRA
142	CN-Din	23.173	112.536	27	20	EBF
143	CN-Du2	42.047	116.284	4	0.45	GRA
144	CH-Oe1	47.286	7.732	1.2	0.5	GRA
145	CN-Dan	30.498	91.066	2.2	0.1	GRA
146	CN-Cha*	42.403	128.096	40	26	MF
147	CA-TP3	42.707	−80.348	16	13.1	ENF

(*continued on next page*)

Table A2 (*continued*)

	Site	Lat	Lon	Measurement Height (m)	Canopy Height (m)	IGBP Class
148	CG-Tch	−4.289	11.656	3.8	1	SAV
149	CA-TP4*	42.71	−80.357	28	21.8	ENF
150	CA-TPD*	42.635	−80.558	35.7	25.7	DBF
151	CA-Obs	53.987	−105.118	25	7.2	ENF
152	CA-TP1	42.661	−80.56	3	2.8	ENF
153	CA-TP2	42.774	−80.459	15	11.1	ENF
154	CA-Oas	53.629	−106.198	39	22	DBF
155	CA-NS6*	55.917	−98.964	8	4	OSH
156	CA-NS5*	55.863	−98.485	9	2	ENF
157	CA-NS7	56.636	−99.948	4.25	0.25	OSH
158	CA-NS4	55.914	−98.381	10	7	ENF
159	CA-Man	55.88	−98.481	30	10	ENF
160	CA-NS3	55.912	−98.382	10	7	ENF
161	CA-NS2	55.906	−98.525	20	16	ENF
162	CA-NS1	55.879	−98.484	24	18	ENF
163	BE-Vie	50.305	5.998	40	35.2	MF
164	CA-Gro	48.217	−82.156	43.3	30	MF
165	BE-Bra	51.308	4.52	42	23	MF
166	BR-Sa1	−2.857	−54.959	57.8	41	EBF
167	AU-Ade	−13.077	131.118	16.5	12.5	WSA
168	AU-TTE	−22.287	133.64	10	4.85	OSH
169	AU-Rob*	−17.118	145.63	40	28	EBF
170	AU-Fog	−12.545	131.307	5.5	1.5	WET
171	AU-Cum	−33.615	150.724	29	24	EBF

The eleven different IGBP land surface classes in this Table include: Wooded Savannas (WSA); Grasslands (GRA); Evergreen Broadleaf Forests (EBF); Crops (CRO); Evergreen Needleleaf Forests (ENF); Savannas (Sav); Deciduous Broadleaf Forests, (DBF); Closed Shrublands (CSH); Mixed Forests (MF); Open Shrublands (OSH); and Permanent Wetlands (WET). Classes for each site were provided by Wang et al. (2020).

References

Andreas, E.L., Jordan, R.E., Mahrt, L., Vickers, D., 2013. Estimating the Bowen ratio over the open and ice-covered ocean. J. Geophys. Res. Oceans 118, 4334–4345. https://doi.org/10.1002/jgrc.20295.

Ayyad, S., Khalifa, M., 2021. Will the Eastern Nile countries be able to sustain their crop production by 2050? An outlook from water and land perspectives. J. Total Environ. 775, 145769 https://doi.org/10.1016/j.scitotenv.2021.145769.

Bouchet, R., 1963. Evapotranspiration reelle et potentielle, signification climatique. Intl. Assoc. Hydrol. Sci. Publ. 62, 134–142.

Brutsaert, W., 2015. A generalized complementary principle with physical constraints for land-surface evaporation. Water Resour. Res. 51 (10), 8087–8093. https://doi.org/10.1002/2015WR017720.

Brutsaert, W., Stricker, H., 1979. An advection-aridity approach to estimate actual regional evapotranspiration. Water Resour. Res. 15 (2), 443–450. https://doi.org/10.1029/WR015i002p00443.

Brutsaert, W., 1982. *Evaporation into the atmosphere: Theory, history, and applications*, Dordrecht. Holland: D. Reidel. https://doi.org/10.1007/978-94-017-1497-6.

Carlowicz, M., 2022. Lake Mead keeps dropping. Earth Observatory. https://earthobservatory. nasa.gov/images/150111/lake-mead-keeps-dropping.

Crago, R., Qualls, R., 2021. A graphical interpretation of the rescaled complementary relationship for evapotranspiration. Water Resour. Res. 57 (8) https://doi.org/10.1029/2020WR028299.

Crago, R., Szilagyi, J., Qualls, R., Huntington, J., 2016. Rescaling the complementary relationship for land surface evaporation. Water Resour. Res. 52 (11), 8461–8471. https://doi.org/10.1002/2016WR019753.

Crago, R., Qualls, R.J., Szilagyi, J., 2022. Complementary relationship for evaporation performance at different spatial and temporal scales. J. Hydrol. 608 (11) https://doi.org/10.1016/j.jhydrol.2022.127575.

European Centre for Medium-Range Weather Forecasts (ECMWF), 2007. IFS documentation–Cy31r1, Part IV: Physical Processes, Shinfield Park, Reading, England.

Gao, B., Xu, X., 2020. Derivation of an exponential complementary function with physical constraints for land surface evaporation estimation. J. Hydrol. 593 https://doi.org/10.1016/j. jhydrol.2020.125623.

Han, S., Tian, F., 2018. Derivation of a sigmoid generalized complementary function for evaporation with physical constraints. Water Resour. Res. 54, 5050–5068. https://doi.org/10.1029/2017WR021755.

Huang, S., Chen, X., Chang, C., Liu, T., Huang, Y., Zan, C., Ma, X., de Maeyer, P., de Voorde, T.V., 2022. Impacts of climate change and evapotranspiration on shrinkage of Aral Sea. Sci. Total Environ. 845, 157203 https://doi.org/10.1016/j.scitotenv.2022.157203.

Huntington, J.L., Szilagyi, J., Tyler, S.W., Pohll, G.M., 2011. Evaluating the complementary relationship for estimating evapotranspiration from arid shrublands. Water Resour. Res. 47, W05533. https://doi.org/10.1029/2010WR009874.

Kahler, D.M., Brutsaert, W., 2006. Complementary relationship between daily evaporation in the environment and pan evaporation. Water Resour. Res. 42, W05413. https://doi.org/10.1029/2005WR004541.

Kaisheng, L., 2022. Contribution of ecological conservation programs and climate change to hydrological regime change in the source region of the Yangtze River in China. Region. Environm. Change 22 (1), 10. https://doi.org/10.1007/s10113-021-01874-z.

la Cecilia, D., Camporese, M., 2022. Resolving streamflow diel fluctuations in a small agricultural catchment with an integrated surface-subsurface hydrological model. Hydrol. Process. 36 (12), e14768.

Lhomme, J.-P., 1997a. An examination of the Priestley-Taylor equation using a convective boundary layer model. Water Resour. Res. 33, 2571–2578.

Lhomme, J.-P., 1997b. A theoretical basis for the Priestley-Taylor coefficient. Boundary-Layer Meteor. 82 (2), 179–191.

Loveland, T.R., Reed, B.C., Brown, J.F., Ohlen, D.O., Zhu, Z., Yang, L., et al., 2000. Development of a Global Land Cover Characteristics Database and IGBP DISCover from 1 km AVHRR Data. Intl. J. Remote Sens. 21 (6–7), 1303–1330. https://doi.org/10.1080/014311600210191.

Ma, N., Szilagyi, J., Zhang, Y., Liu, W., 2019. Complementary-relationship-based modeling of terrestrial evapotranspiration across China during 1982-2012: Validations and spatiotemporal analyses. *J. Geophys. Res.: Atmos.*, 124. https://doi.org/2018JD029850.

Ma, N., Szilagyi, J., Zhang, Y., 2021. Calibration-free complementary relationship estimates terrestrial evapotranspiration globally. *Water Resour. Res.*, 57, e2021WR029691. https://doi.org/10.1029/2021WR029691.

Ma, N., Szilagyi, J., 2019. The CR of evaporation: a calibration-free diagnostic and benchmarking tool for large-scale terrestrial evapotranspiration modeling. Water Resour. Res. 55 https://doi.org/10.1029/2019WR024867.

Ma, N., Zhang, Y., Szilagyi, J., Guo, Y., Zhai, J., Gao, H., 2015. Evaluating the complementary relationship of evapotranspiration in the alpine steppe of the Tibetan Plateau. Water Resour. Res. 51, 1069–1083. https://doi.org/10.1002/2014WR015493.

Ma, N., Szilagyi, J., Jozsa, J., 2020. Benchmarking large-scale evapotranspiration estimates: A perspective from a calibration-free complementary relationship approach and FLUXCOM. J. Hydrol. 590 https://doi.org/10.1016/j.jhydrol.2020.125221.

Mahmood, R., Jia, S., 2019. Assessment of hydro-climatic trends and causes of dramatically declining stream flow to Lake Chad, Africa, using a hydrological approach. J. Total Environ. 675, 122–140. https://doi.org/10.1016/j.scitotenv.2019.04.219.

Mauder, M., Foken, T., Cuxart, J., 2020. Surface-energy budget closure over land: A review. Boundary-Layer Meteor. 177, 395–426. https://doi.org/10.1007/s10546-020-00529-6.

Maxmen, A., 2018. As Cape Town water crisis deepens, scientists prepare for 'Day Zero'. Nature 554, 13–14. https://doi.org/10.1038/d41586-018-01134-x.

McVicar, T.R., Jupp, D.L.B., 2002. Using covariates to spatially interpolate moisture availability in the Murray-Darling Basin: A novel use of remotely sensed data. Remote Sens. Environ. 79, 199–212.

Monteith, J.L., 1981. Evaporation and surface temperature. Quart. J. Royal Meteor. Soc. 107 (451), 1–27. https://doi.org/10.1002/qj.49710745102.

Morton, F.I., 1983. Operational estimates of areal evapotranspiration and their significance to the science and practice of hydrology. J. Hydrol. 66, 1–76.

Morton, F.I., Ricard, F., Fogarasi, F., 1985. Operational estimates of areal evapotranspiration and lake evaporation—Program WREVAP. NHRI Paper 24, National Hydrologic. Research Institute, Saskatoon, Canada.

Palmer, M. A., Filoso, S., Fanelli, R. M., 2014. From ecosystems to ecosystem services: Stream restoration as ecological engineering. *Ecol. Engin.*, 65, 62-70. https://doi.org/10.1016/j.ecoleng.2013.07.059.

Pastorello, G., Trotta, C., Canfora, E., Chu, H., Christianson, D., Cheah, Y.W., Poindexter, C., Chen, J., Elbashandy, A., Humphrey, M., Isaac, P., 2020. The FLUXNET2015 dataset and the ONEFlux processing pipeline for eddy covariance data. Sci. Data 7 (1), 225. https://doi.org/10.1038/s41597-020-0534-3.

Penman, H.L., 1948. Natural evaporation from open water, bare soil and grass. Proc. Royal Soc. A: Math. Phys. Eng. Sci. 193, 120–145. https://doi.org/10.1098/rspa.1948.0037.

Priestley, C.H.B., Taylor, R.J., 1972. On the assessment of surface heat flux and evaporation using large-scale parameters. Monthly Weather Rev. 100 (2), 81–92.

Reichstein, M., Falge, E., Baldocchi, D., Papale, D., Aubinet, M., et al., 2005. On the separation of net ecosystem exchange into assimilation and ecosystem respiration: review and improved algorithm. Global Change Biol. 11, 1424–1439.

Rezaei, A., Gurdak, J.J., 2020. Large-scale climate variability controls on climate, vegetation coverage, lake and groundwater storage in the Lake Urmia watershed using SSA and wavelet analysis. J. Total Environ. 724, 138273 https://doi.org/10.1016/j.scitotenv.2020.138273.

Stull, R., 1988. An introduction to boundary layer meteorology. Kluwer Academic, Dordrecht, Holland.

Stull, R., 2000. Meteorology for Scientists and Engineers. Brooks/Cole, Pacific Grove, CA, USA.

Susnik, J., Masia, S., Kravcik, M., Pokorny, J., Hesslerova, P., 2022. Costs and benefits of landscape-based water retention measures as nature-based solutions to mitigating climate impacts in eastern Germany, Czech Republic, and Slovakia. Land Degrad. Develop. 33 (16), 3074–3087. https://doi.org/10.1002/ldr.4373.

Szilagyi, J., 2014. Temperature corrections in the Priestley-Taylor equation of evaporation. J. Hydrol. 519, 455–464. https://doi.org/10.1016/j.jhydrol.2014.07.040.

Szilagyi, J., 2015. Complementary relationship-based 30-year normals (1981–2010) of monthly latent heat fluxes across the contiguous United States, *Water Resour.* Res. 51, 9367–9377. https://doi.org/10.1002/2015WR017693.

Szilagyi, J., 2018. A calibration-free, robust estimation of monthly land surface evapotranspiration rates for continental-scale hydrology. Hydrol. Res. 49 https://doi.org/10.2166/nh.2017.078.

Szilagyi, J., 2021. On the thermodynamic foundations of the complementary relationship of evaporation. J. Hydrol. 593, 125916 https://doi.org/10.1016/j.jhydrol.2020.125916.

Szilagyi J., Parlange, M. B., Katul, G. G., 2014. Assessment of the Priestley-Taylor parameter value from ERA-Interim global reanalysis data. *J. Hydrol. Environ. Res.*, 2 (1), 1-7. https://snr.unl.edu/szilagyi/Szilagyi et al_off print.pdf.

Szilagyi, J., Jozsa, J., 2008. New findings about the complementary relationship-based estimation methods. J. Hydrol. 354 (1–4), 171–186. https://doi.org/10.1016/j.jhydrol.2008.03.008.

Szilagyi, J., Crago, R., Qualls, R., 2017. A calibration-free formulation of the complementary relationship of evaporation for continental-scale hydrology. J. Geophys. Res.: Atmos. 122 (1), 264–278. https://doi.org/10.1002/2016JD025611.

Szilagyi, J., Ma, N., Crago, R. D., Qualls, R. J., 2022. Power-function expansion of the polynomial complementary relationship of evaporation, *Water Resour. Res.*, 58(11), e2022WR033095. https://doi.org/10.1029/2022WR033095.

Wang, L., Tian, F., Han, S., Wei, Z., 2020. Determinants of the asymmetric parameter in the generalized complementary principle of evaporation. Water Resour. Res. 56 https://doi.org/10.1029/2019WR026570.

Ward, F.A., 2022. Integrating water science, economics, and policy for future climate adaptation. J. Environ. Managem. 325 (B), 116574 https://doi.org/10.1016/j.jenvman.2022.116574.

World Meteorological Organization (WMO), 2021. State of the global climate, 2021. WMO-No. 1290. Accessible at https://library.wmo.int.